

**Bifunctional Antioxidant for Concurrent Enhancement of Stability
and Zinc-ion Storage Properties of $Ti_3C_2T_x$**

Jie Wang, Guohao Li, Hailiang He, Xiaohui Li, Jiale Fan, Yingxinjie Wang, Xiuqiang Xie*, and Nan Zhang*

J. Wang., G. Li., H. He., X. Li., J. Fan., Y. Wang., Prof. X. Xie, Prof. N. Zhang
College of Materials Science and Engineering, Hunan University, Changsha 410082,
P. R. China

E-mail: xiuqiang_xie@hnu.edu.cn; nanzhang@hnu.edu.cn

Content list

Figure S1. Chemical composition of M and SM.....	4
Figure S2. High-resolution S 2p XPS spectra of SM.....	5
Figure S3. LSV curves of NaBH ₄ , Na ₂ S, NaAc, VC, NaHSO ₃ , and NaCl.....	6
Figure S4. Optical images of the mixed Ti ₃ C ₂ T _x and rGO colloidal suspensions with different reductants.....	7
Figure S5. XPS survey spectra of MG and SMG.....	8
Figure S6. High-resolution Ti 2p XPS spectra of MG and SMG.	9
Figure S7. High-resolution S 2p XPS spectra of SMG.....	10
Figure S8. Characterization of MG and SMG after storing in H ₂ O for 15 days. (A) XRD and (B) Raman of MG and SMG.....	11
Figure S9. N ₂ adsorption/desorption isotherms of SMG and MG samples.	12
Figure S10. Typical SEM image of MG.	13
Figure S11. GCD curves of (A) MG and (B) SMG electrodes at different current densities.....	14
Figure S12. Nyquist plots of (A) SMG and (B) MG electrodes.	15
Figure S13. CV curves of MG and SMG electrodes at different scan rates.	16
Figure S14. The linear relationship of the reductive (R) and oxidative (O) peak current (I _p) and the square root of the scan rate (v ^{1/2}) for the MG electrode.....	17
Figure S15. Log(i) vs. log(v) linear plots at reductive (R) and oxidative (O) peaks of the MG electrode.....	18
Figure S16. Capacitance-contribution percentage at different scan rates of the MG electrode.	19
Figure S17. CV curve of the MG electrode at 10 mV s ⁻¹ with the estimated capacitive contribution in the orange region.	20
Figure S18. Area specific capacitance and capacitance retention of SMG compared with a series of reported MXene-based materials for zinc-ion storage performance. ²⁻⁷	21
Figure S19. The Ragone plot of the device compared with other works. ^{3, 4, 8-13}	22

Table S1 Comparison of capacitance and capacitance retention of MXene-based materials for zinc-ion storage.	23
Table S2. Comparison of energy density and power density of MXene-based materials for zinc-ion storage.	24

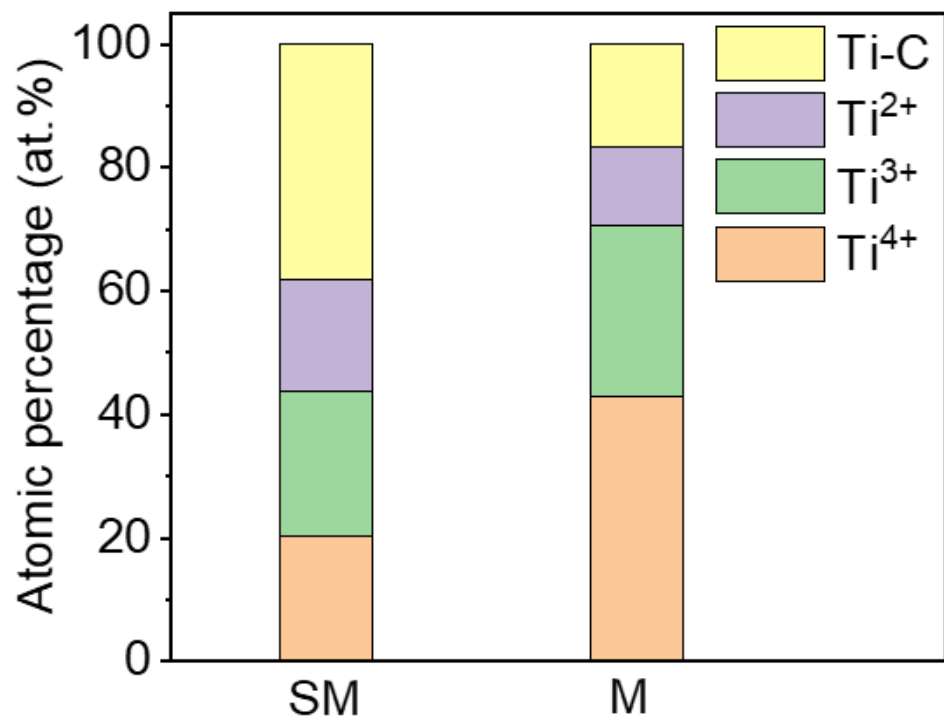


Figure S1. Chemical composition of M and SM.

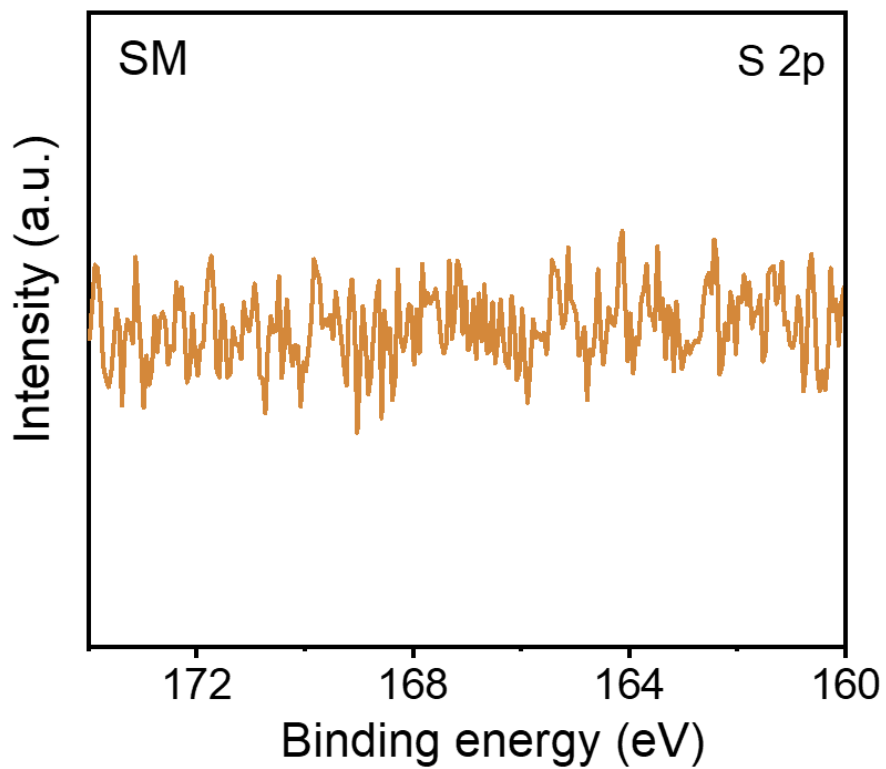


Figure S2. High-resolution S 2p XPS spectra of SM.

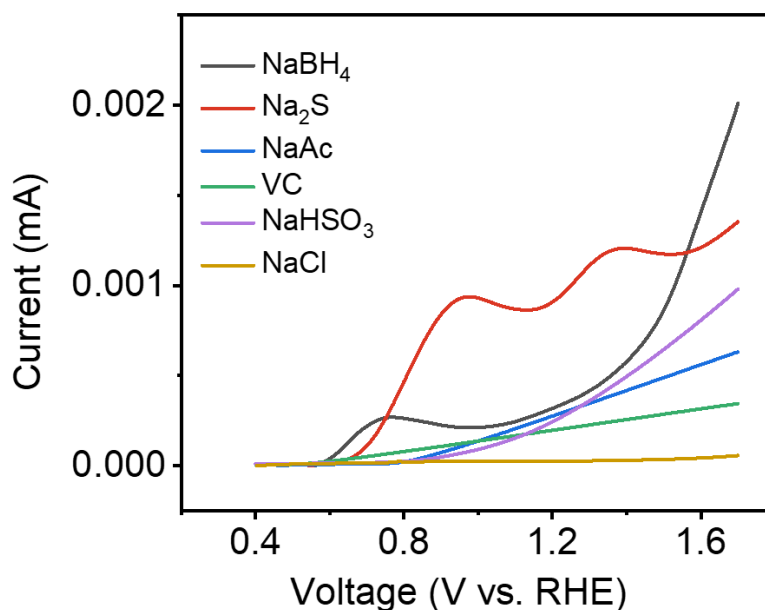


Figure S3. LSV curves of NaBH₄, Na₂S, NaAc, VC, NaHSO₃, and NaCl.

A three-electrode system was used to collect the linear sweep voltammetry (LSV) curves to measure redox behaviors of reagents, including NaBH₄, Na₂S, NaAc, VC, NaHSO₃, and NaCl. Before the test, N₂ is introduced into the electrolytic cell for 30 minutes to remove oxygen in the solution, thereby preventing oxygen from interfering with the test results. For the tests involving NaBH₄ and Na₂S, the working electrode was carbon cloth, the counter electrode was a graphite rod, and the reference electrode was Hg/HgO. For NaAc, VC, NaHSO₃, and NaCl, the counter electrode was platinum foil, and the reference electrode was Ag/AgCl. According to the Nernst equation, the potentials vs. reversible hydrogen electrode (RHE) were calculated using the following formulas by measuring the pH of each solution at 25 °C:

$$E_{\text{RHE}} = E_{\text{Ag/AgCl}} + 0.197 + 0.059 \text{ pH}$$

$$E_{\text{RHE}} = E_{\text{Hg/HgO}} + 0.098 + 0.059 \text{ pH}$$

NaBH₄ exhibits an oxidation peak at 0.767 V (vs. RHE), while Na₂S features two oxidation peaks at 0.975 and 1.398 V (vs. RHE). This more negative oxidation potential of NaBH₄ demonstrates that NaBH₄ possesses stronger reducing power than Na₂S.¹ In contrast, no oxidation peaks were observed for NaAc, VC, NaHSO₃, or NaCl, suggesting their reduction strength is weaker than Na₂S. Therefore, Na₂S has a moderate reduction strength among the reducing agents used in the work, which promotes the synthesis of the SMG (**Figure S4**).

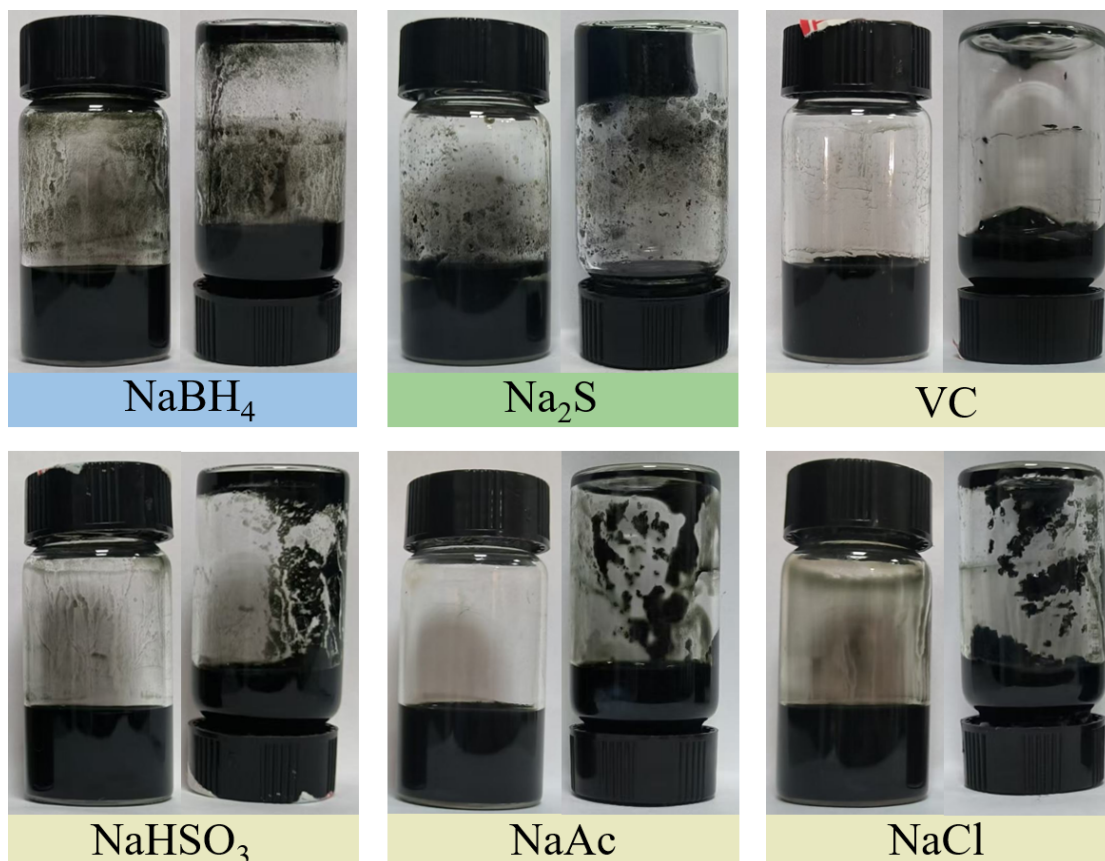


Figure S4. Optical images of the mixed $\text{Ti}_3\text{C}_2\text{T}_x$ and rGO colloidal suspensions with different reductants.

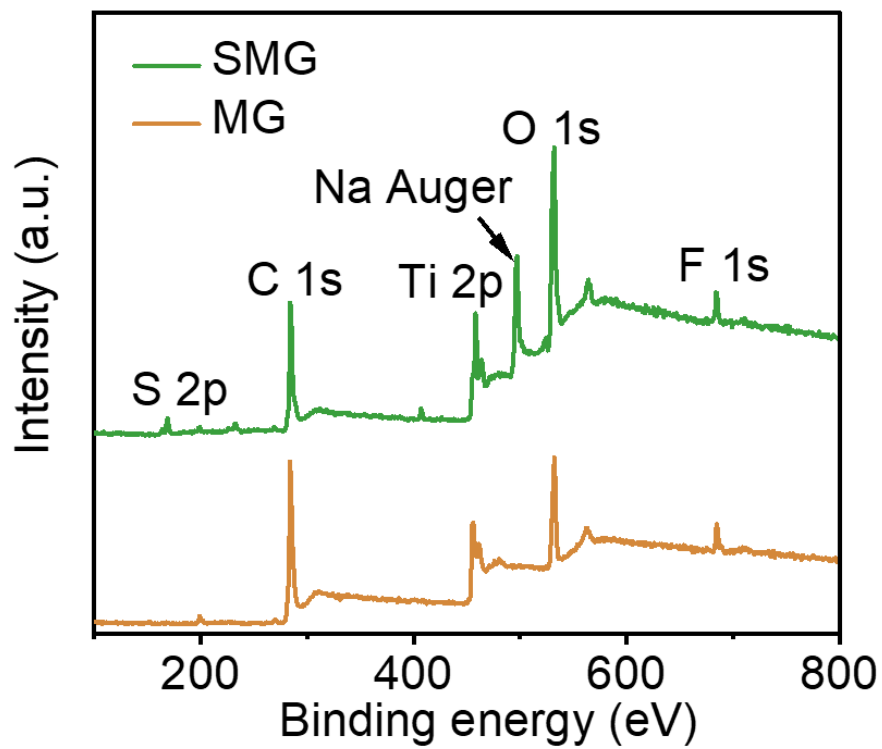


Figure S5. XPS survey spectra of MG and SMG.

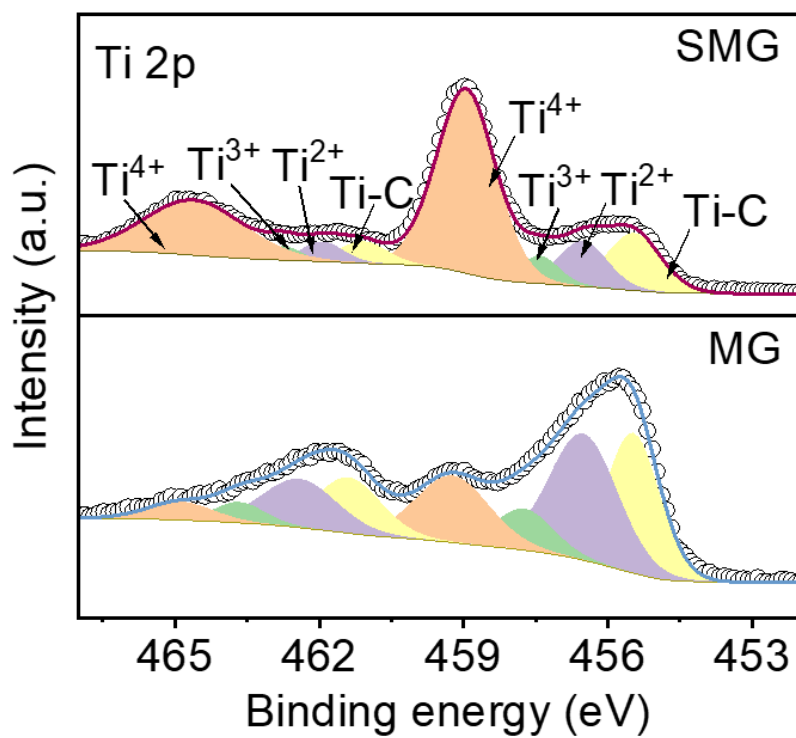


Figure S6. High-resolution Ti 2p XPS spectra of MG and SMG.

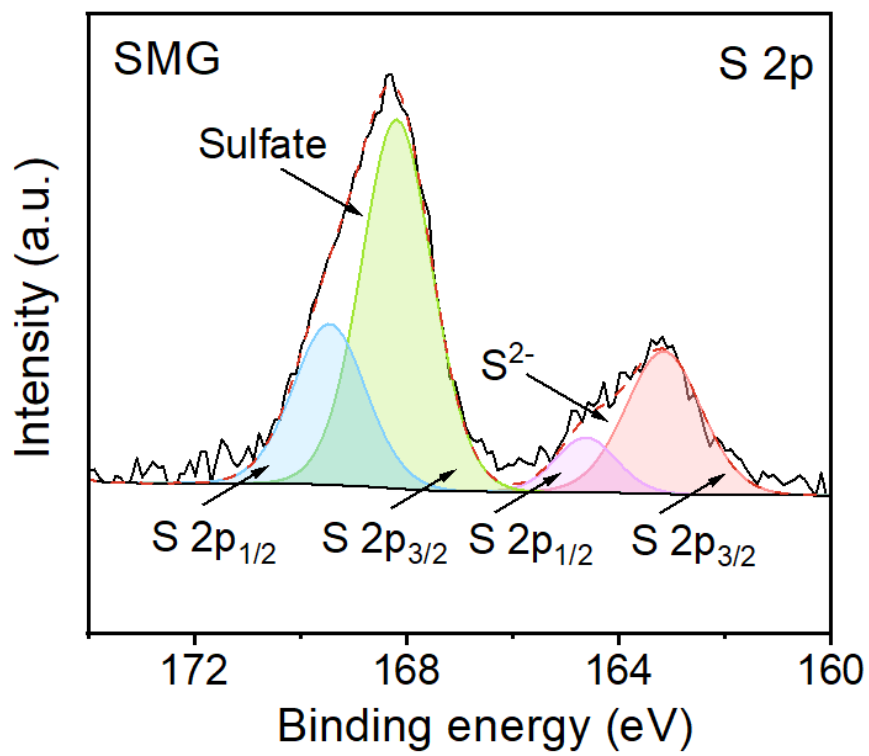


Figure S7. High-resolution S 2p XPS spectra of SMG.

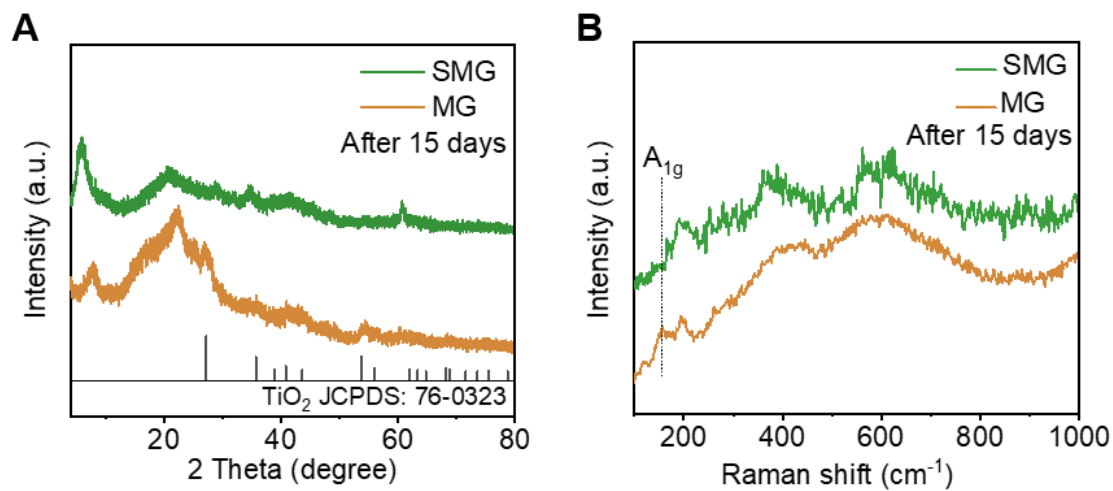


Figure S8. Characterization of MG and SMG after storing in H₂O for 15 days. (A) XRD and (B) Raman of MG and SMG.

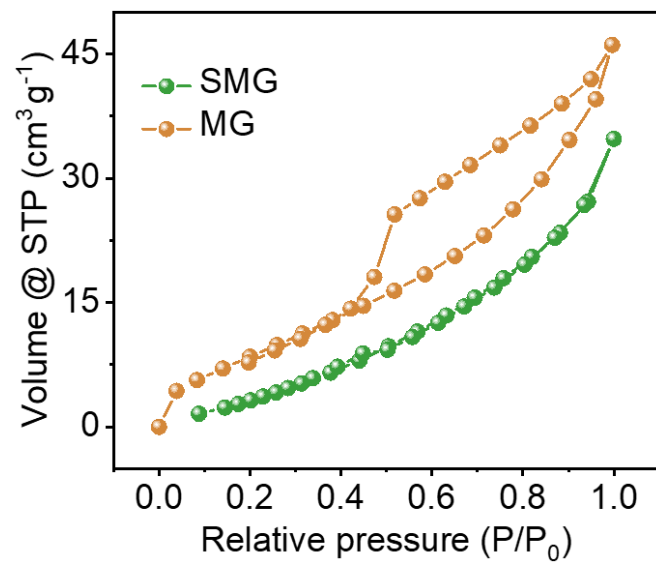


Figure S9. N₂ adsorption/desorption isotherms of SMG and MG samples.

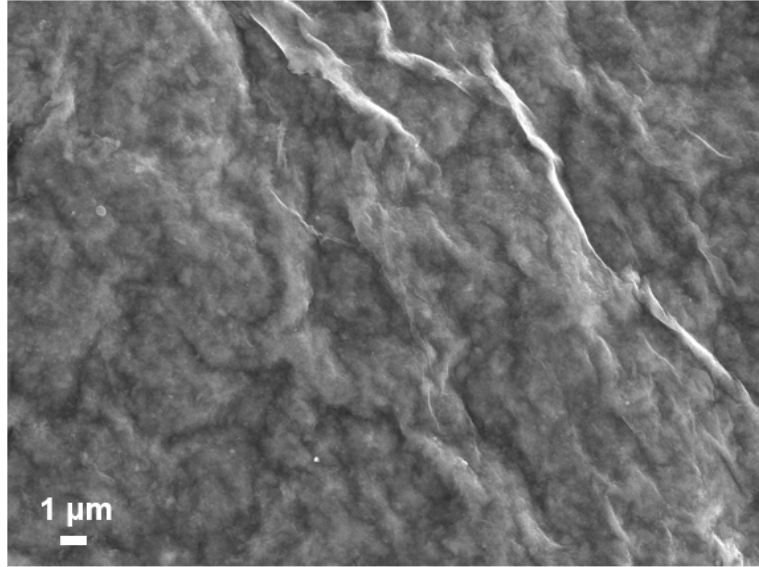


Figure S10. Typical SEM image of MG.

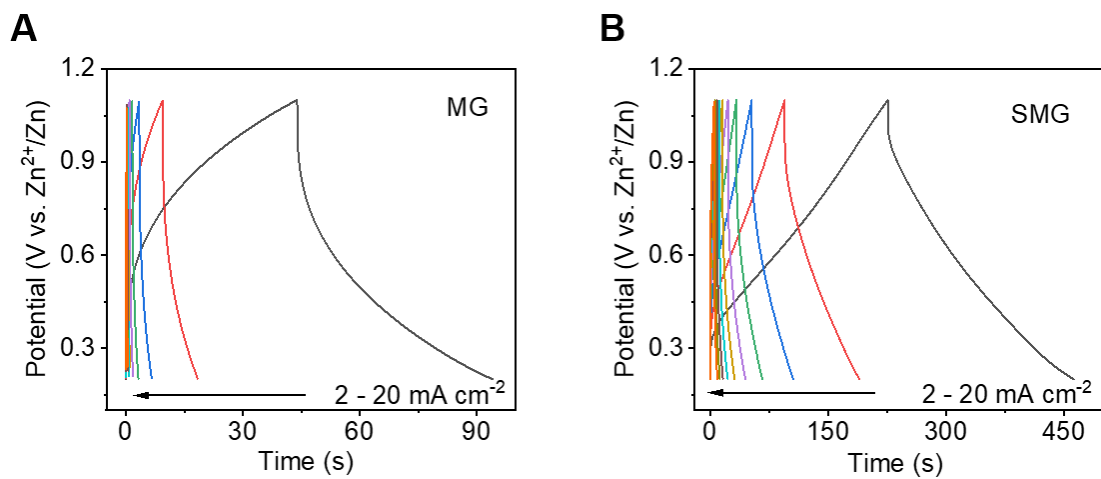


Figure S11. GCD curves of (A) MG and (B) SMG electrodes at different current densities.

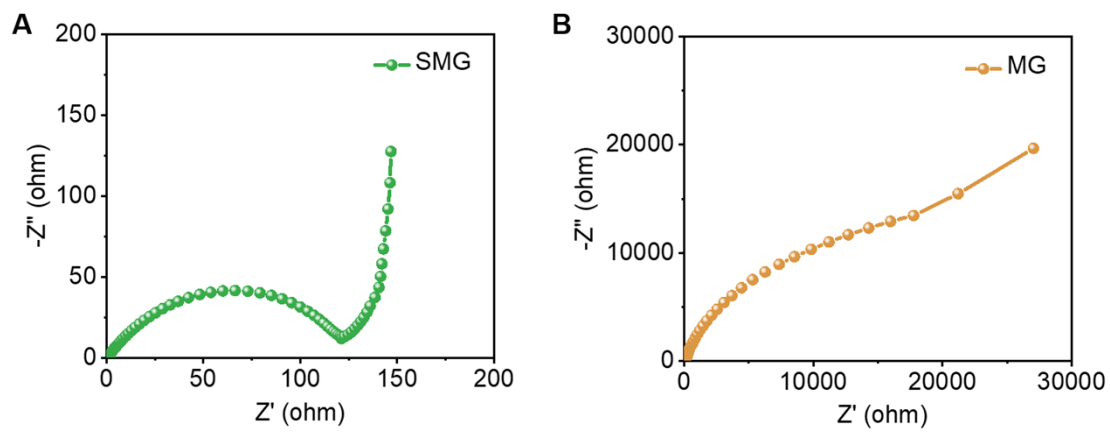


Figure S12. Nyquist plots of (A) SMG and (B) MG electrodes.

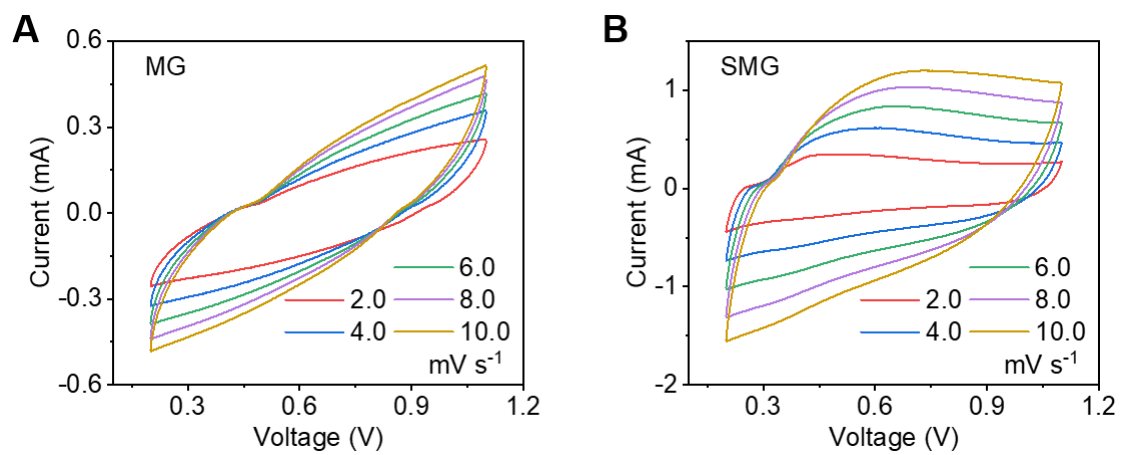


Figure S13. CV curves of MG and SMG electrodes at different scan rates.

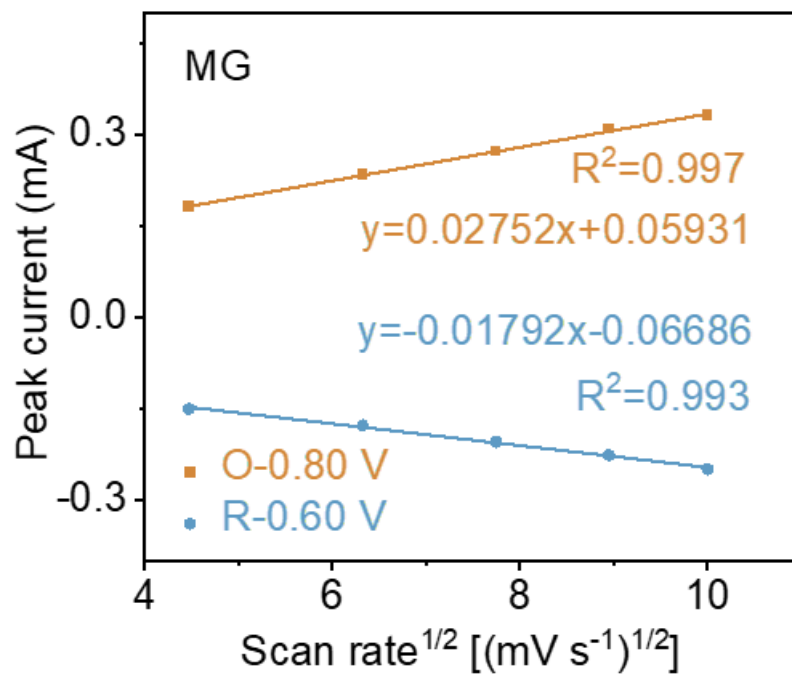


Figure S14. The linear relationship of the reductive (R) and oxidative (O) peak current (I_p) and the square root of the scan rate ($v^{1/2}$) for the MG electrode.

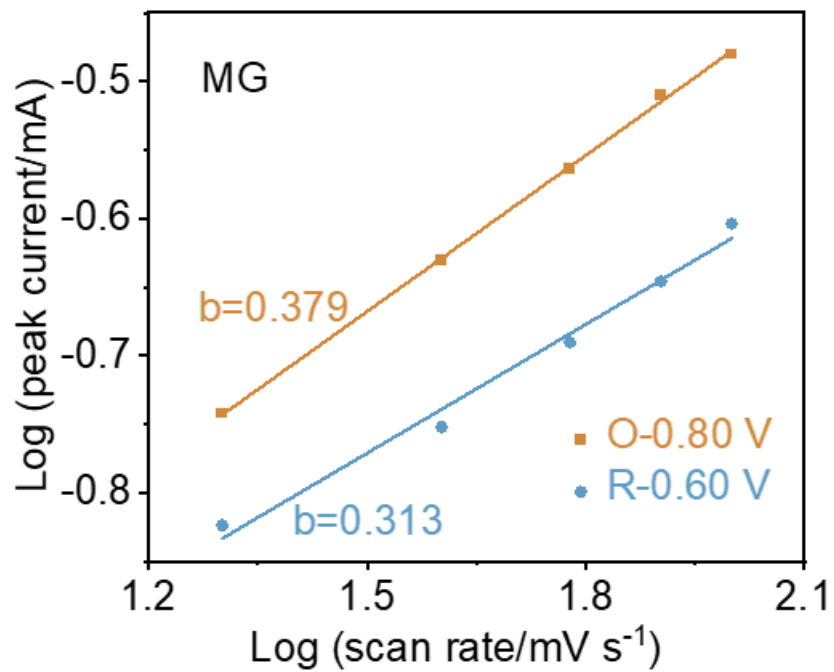


Figure S15. Log(*i*) vs. log(*v*) linear plots at reductive (R) and oxidative (O) peaks of the MG electrode.

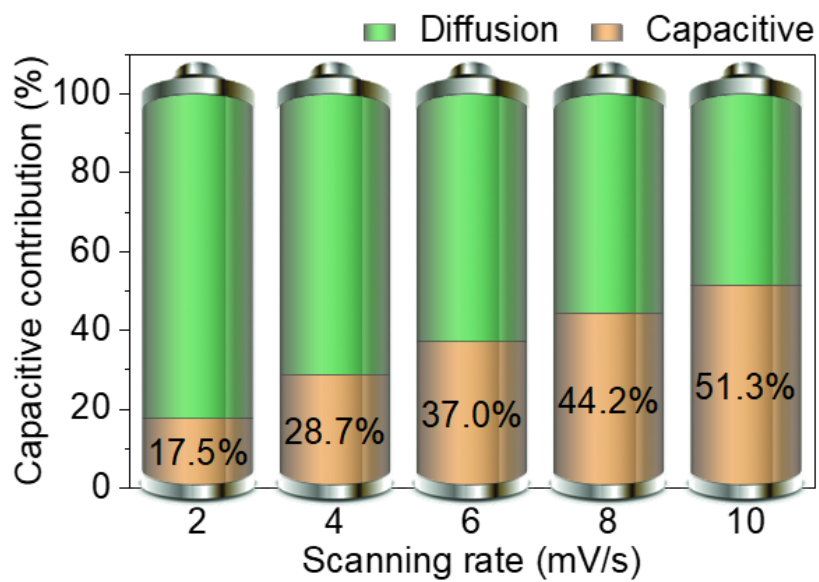


Figure S16. Capacitance-contribution percentage at different scan rates of the MG electrode.

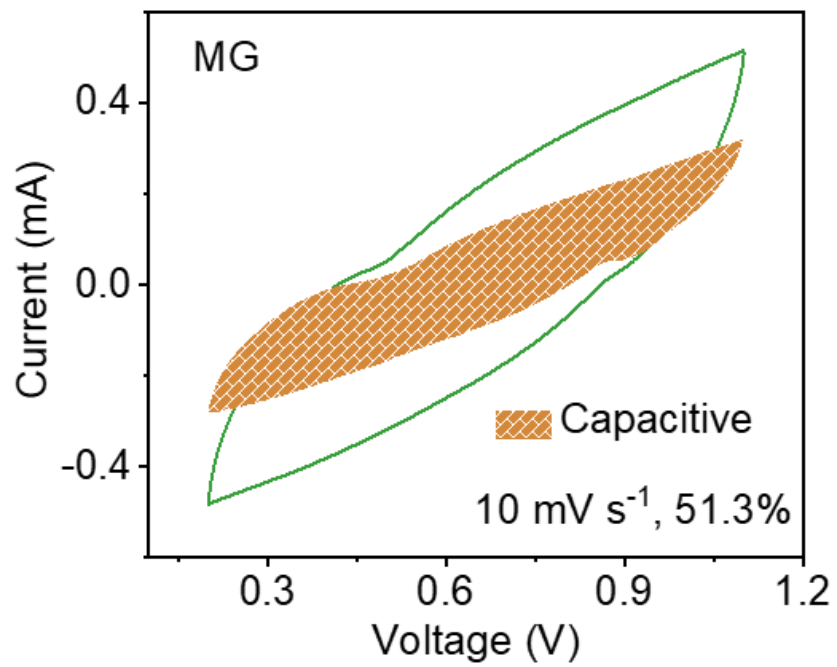


Figure S17. CV curve of the MG electrode at 10 mV s⁻¹ with the estimated capacitive contribution in the orange region.

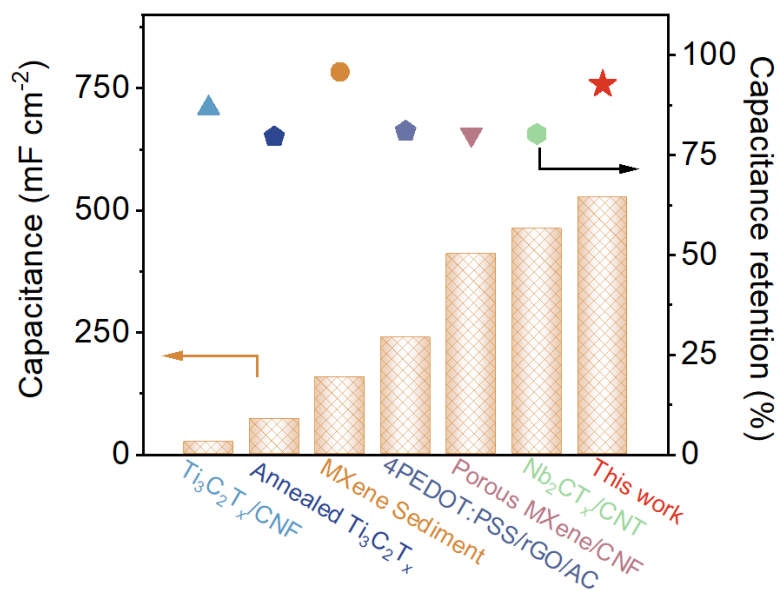


Figure S18. Area specific capacitance and capacitance retention of SMG compared with a series of reported MXene-based materials for zinc-ion storage performance. ²⁻⁷

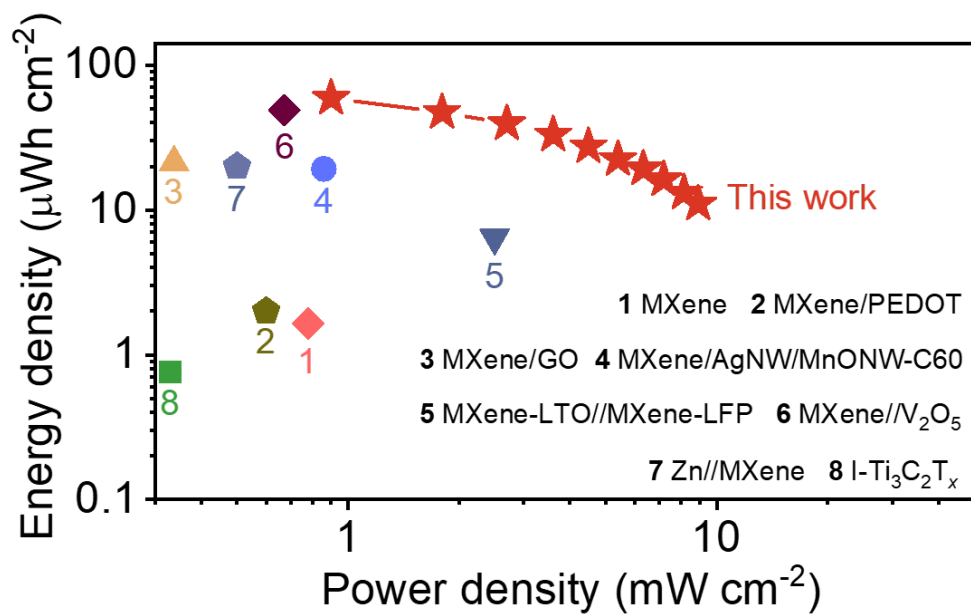


Figure S19. The Ragone plot of the device compared with other works.^{3, 4, 8-13}

Table S1 Comparison of capacitance and capacitance retention of MXene-based materials for zinc-ion storage.

Material	Capacitance (mF cm ⁻²)	Capacitance retention (%)	Ref
Ti ₃ C ₂ T _x /CNF	25.3	86.8	2
Annealed Ti ₃ C ₂ T _x	72	79.6	3
MXene Sediment	158	95.8	4
4PEDOT:PSS/rGO/ AC	239	81	5
Porous MXene/CNF	410	80.2	6
Nb ₂ CT _x /CNT _x	462	80.3	7
SMG	526.2	92.7	This work

Table S2. Comparison of energy density and power density of MXene-based materials for zinc-ion storage.

Material	Energy density ($\mu\text{Wh cm}^{-2}$)	Power density (mW cm^{-2})	Ref
MXene	1.64	0.78	4
MXene/PEDOT	2.00	0.60	8
MXene/GO	21.3	0.34	9
MXene/AgNW/MnONW-C60	19.2	0.86	10
MXene-LTO//MXene-LFP	6.40	2.50	11
MXene/ V_2O_5	48.90	0.67	12
Zn//MXene	20.0	0.50	3
I- $\text{Ti}_3\text{C}_2\text{T}_x$	0.76	0.33	13
SMG	59.20	0.90	This work
	11.03	8.92	

References

1. Y. Hua, Y. Sun, F. Yan, S. Wang, Z. Xu, B. Zhao and Z. Zhang, Ionization potential-based design of deep eutectic solvent for recycling of spent lithium ion batteries, *Chem. Eng. J.*, 2022, **436**, 133200.
2. W. Tian, A. VahidMohammadi, M. S. Reid, Z. Wang, L. Ouyang, J. Erlandsson, T. Pettersson, L. Wågberg, M. Beidaghi and M. M. Hamed, Multifunctional nanocomposites with high strength and capacitance using 2D MXene and 1D nanocellulose, *Adv. Mater.*, 2019, **31**, 1902977.
3. L. Li, W. Liu, K. Jiang, D. Chen, F. Qu and G. Shen, In-situ annealed $Ti_3C_2T_x$ MXene based all-solid-state flexible Zn-ion hybrid micro supercapacitor array with enhanced stability, *Nano-Micro Lett.*, 2021, **13**, 1-11.
4. S. Abdolhosseinzadeh, R. Schneider, A. Verma, J. Heier, F. Nüesch and C. Zhang, Turning trash into treasure: additive free MXene sediment inks for screen-printed micro-supercapacitors, *Adv. Mater.*, 2020, **32**, 2000716.
5. X. Tian, S. Zhao, Y. Gao, H. Li, W. Cao and B. Xu, 3D printing-directed synergistic design of high-performance zinc-ion hybrid capacitors and nanogenerators for all-in-one self-powered energy wristband, *Adv. Funct. Mater.*, 2023, **33**, 2300381.
6. M. Wang, Y. Cheng, H. Zhang, F. Cheng, Y. Wang, T. Huang, Z. Wei, Y. Zhang, B. Ge and Y. Ma, Nature-inspired interconnected macro/meso/micro-porous MXene electrode, *Adv. Funct. Mater.*, 2023, **33**, 2211199.
7. J. Xiao, J. Wen, J. Zhao, X. Ma, H. Gao and X. Zhang, A safe etching route to synthesize highly crystalline Nb_2CT_x MXene for high performance asymmetric supercapacitor applications, *Electrochim. Acta*, 2020, **337**, 135803.
8. P. Das, X. Shi, Q. Fu and Z. S. Wu, Substrate-free and shapeless planar micro-supercapacitors, *Adv. Funct. Mater.*, 2020, **30**, 1908758.
9. H. Zhang, Z. Wei, J. Wu, F. Cheng, Y. Ma, W. Liu, Y. Cheng, Y. Lin, N. Liu and Y. Gao, Interlayer-spacing-regulated MXene/rGO foam for multi-functional zinc-ion microcapacitors, *Energy Storage Mater.*, 2022, **50**, 444-453.
10. X. Li, H. Li, X. Fan, X. Shi and J. Liang, 3D-printed stretchable micro-supercapacitor with remarkable areal performance, *Advanced Energy Materials*, 2020, **10**, 1903794.
11. S. Zheng, H. Wang, P. Das, Y. Zhang, Y. Cao, J. Ma, S. Liu and Z. S. Wu, Multitasking MXene inks enable high-performance printable microelectrochemical energy storage devices for all-flexible self-powered integrated systems, *Adv. Mater.*, 2021, **33**, 2005449.
12. X. Li, Y. Ma, Y. Yue, G. Li, C. Zhang, M. Cao, Y. Xiong, J. Zou, Y. Zhou and Y. Gao, A flexible Zn-ion hybrid micro-supercapacitor based on MXene anode and V_2O_5 cathode with high capacitance, *Chem. Eng. J.*, 2022, **428**, 130965.
13. C. Zhang, M. P. Kremer, A. Seral-Ascaso, S. H. Park, N. McEvoy, B. Anasori, Y. Gogotsi and V. Nicolosi, Stamping of flexible, coplanar micro-supercapacitors using MXene inks, *Adv. Funct. Mater.*, 2018, **28**, 1705506.

